ACTA IMEKO
ISSN: 2221-870X
March 2022, Volume 11, Number 1, 1 - 7

Feasibility and performance analysis in 3D printing of artworks using laser scanning microprofilometry

Sara Mazzocato[1], Giacomo Marchioro[2], Claudia Daffara[1]

[1] *Department of Computer Science, University of Verona, str. le Grazie 15, I-37134, Verona, Italy*
[2] *Department of Cultures and Civilisations, University of Verona, v.le dell'Università 4, I-37129, Verona, Italy*

ABSTRACT
We investigated optical scanning microprofilometry and conoscopic holography sensors as nondestructive testing and evaluation tools in archeology for obtaining an accurate 3D printed reproduction of the data. The modular microprofilometer prototype allows a versatile acquisition of different materials and shapes producing a high-quality dataset that enables surface modelling at micrometric scales from which a "scientific" replica can be obtained through 3D printing technologies. As exemplar case study, an archeological amphora was acquired and 3D printed. In order to test the feasibility and the performance of the whole process chain from the acquisition to the reproduction, we propose a statistical multiscale analysis of the surface signal of object and replica based on metrological parameters. This approach allows to demonstrate that the accuracy of the 3D printing process preserves the range of spatial wavelengths that characterizes the surface features of interest within the technology capabilities. This work extends the usefulness of the replicas from museum exposition to scientific applications.

Section: RESEARCH PAPER

Keywords: Optical profilometry; 3D printing; conoscopic holography; surface analysis; non-destructive testing

Citation: Sara Mazzocato, Giacomo Marchioro, Claudia Daffara, Feasibility and performance analysis in 3D printing of artworks using laser scanning microprofilometry, Acta IMEKO, vol. 11, no. 1, article 19, March 2022, identifier: IMEKO-ACTA-11 (2022)-01-19

Section Editor: Fabio Santaniello, University of Trento, Italy

Received March 7, 2021; **In final form** March 22, 2022; **Published** March 2022

Funding: This work was partially supported by SCAN4RECO project, European Union Horizon 2020 Framework Programme for Research and Innovation, grant agreement no 665091 and by TEMART project, POR FESR 2014-2020.

Corresponding author: Sara Mazzocato, e-mail: sara.mazzocato@univr.it

1. INTRODUCTION

3D sensors and 3D printing technologies are gaining more and more attention in many fields, from industry to medicine, to cultural heritage [1]-[5] also thanks to fact that 3D printers are being easily accessible and have gradually gained better levels of accuracy. In the field of cultural heritage, these technologies arouse interest because of the possibility to reproduce artworks or part of them for museum exhibition, restoration and conservation reasons, haptic fruition, and other purposes [6]-[8].

Clearly, the first step to obtain realistic and accurate 3D printed objects is the data acquisition process. In this context, non-contact 3D optical systems play an important role in such applications, from quality control to robotics, where a remote measurement is preferable and/or the object is fragile. Their capability to measure the surfaces in contact-less and non-invasive way led them to be key instruments especially in the field of cultural heritage, where the surface of the object or the 3D shape at the various scales is the central and essential part of the artwork itself [9]-[14] and integrated diagnostics is performed [15]. Each surface has an intrinsic multiscale nature that can be represented as a superimposition of a large number of spatial wavelengths. The natural question that arises spontaneously is if (and the extent to which) the 3D printing process preserves this intrinsic multiscale nature of the surface. Despite the rapid growth of the use of 3D printing technologies, the accuracy of the 3D printed models has not been thoroughly investigated and not all the technologies are studied [16]-[19].

In this paper, we first present the prototype of the optical scanning microprofilometer as scanning system that allows high accuracy acquisition of the object [20]. The system is based on the interferometric method of conoscopic holography that enables to acquire surface data with micrometric resolution. Thanks to the adaptability of the conoscopic holography sensors and the scanning setup, the system is able to measure irregular shapes, composite materials, and polychrome surfaces, thus

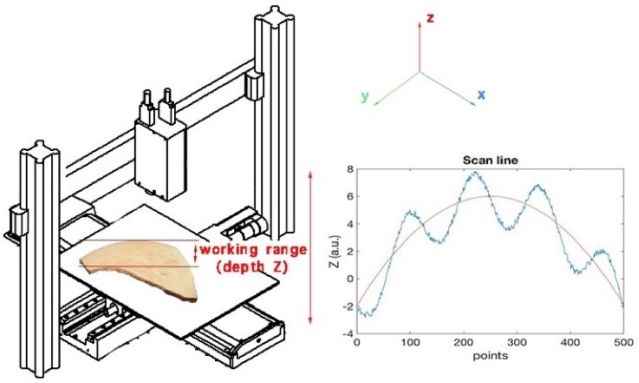

Figure 1. Scanning setup of the microprofilometer with the specification of the working range and an exemplification of a scan line.

leading to a multiscale and multimaterial approach in surface analysis [21].

Here, the scanning profilometry is used to acquire accurate data of an archaeological object, which are then processed in order to obtain a 3D printed replica of the object itself. Thus, we have come full circle by measuring the 3D printed object and by comparing the surfaces on a metrological basis.

After a brief presentation of the optical microprofilometer developed in our laboratory (section 2), we demonstrate the application in a real case study, processing the dataset acquired on an ancient amphora and obtaining a mesh file suitable for the 3D printer (section 3). In section 4 we propose a statistical and multiscale analysis of the original object and its 3D printed replica in order to assess the accuracy of the whole process from the acquisition to the 3D printing. Finally, in the concluding section, the main results are discussed.

2. OPTICAL MICROPROFILOMETRY

The optical microprofilometer is based on the conoscopic holography technique that exploits interference patterns to obtain a pointwise measurement of distances with micrometric accuracy [22], [23]. In detail, a laser backscattered from the surface is splitted into ordinary and extraordinary rays after passing through an optically anisotropic crystal. The two beams share the same geometric paths but have orthogonal polarization modes. The refractive index of the crystal depends on the angle of incidence of the beam and on its polarization state determining a difference in the optical path lengths. Once the two beams exit the crystal, they interfere to each other, and the pattern is recorded. The analysis of the generated pattern allows to obtain information about the distance of the sampled surface from the light source [5], [6].

Conoscopic holography sensors enable to perform contactless measurements at sub-millimeter spatial resolution with a precision down to a few micrometers on different kind of materials, from the specular reflective surfaces to the diffusive ones. The developed system has a multi-probe module including a sensor for diffusive materials, a sensor for reflective materials, and a sensor for specular or transparent surfaces (all sensors by Optimet). Interchangeable lenses allow performing acquisitions in different working ranges, i.e., the maximum scanned height, tailored to the scale of the object. This aspect is very important in profilometry applied to the variegate 3D archaeological manufacts.

The different combination of sensors and lenses allows the analysis of reflective materials with a maximum accuracy of 1 μm and working range of 1 mm up to a working range of 9 mm with an accuracy of 4.5 μm. While for diffusive material it is possible to achieve an accuracy of 2 μm with a working range limited to 0.6 mm or extending the working range up to 180 mm maintaining a sub-millimeter accuracy of 100 μm.

The surface dataset is obtained as sequence of single point measurements of the depth distance (Z) in the X-Y plane, with the probe triggered to a set of motorized stages moving the object plate, as can be seen in Figure 1. The advantage is the creation of profiles and surface maps with custom "field of view" that is only limited by the axis range. Our scanning setup is composed by a motion system with linear micrometric axis stages (by PI) orthogonally mounted to form the acquisition grid (X, Y axis). The axes have a maximum travel range of 300 mm and a step precision of 0.1 μm with an accuracy of 1 μm over the entire length. The probe operates in pulse-mode, receiving pulses from an external trigger sent by the scanning system: for each pulse the sensor measures the distance to the sampled object. As depicted in Figure 1 the object surface is effectively measured within maximum the working range of the depth sensor. In order to improve the capability of scanning complex shapes, a third motorized axis controlling the position of the probe along the line of sight can be added.

3. SURFACE ACQUISITION AND 3D PRINTING

The case study concerns a portion of an archaeological amphora (Figure 2).

The object is acquired with the ConoPoint-3 sensor with a 75mm lens. This probe-lens coupling allows a working range of 18 mm with a stand-off distance of 70 mm and a laser spot size of 47 μm. We acquired a selected region of interest of 55.2×80.1 mm^2 with a scanning step (X-Y sampling grid) of 100 μm.

The interest in this case arises from its surface geometrical structure being a superimposition of a large number of scales. The usual approach in surface metrology is to separate the surface in three main scales: the roughness, that represents the irregularities at smaller wavelengths and exhibits a random nature often related to the behaviour of the material; the waviness, i.e. the more widely spaced variation often associated with the traces left by the tools used for the creation of the object; and the form, i.e. the 3D shape of the object. Obviously, even if these features are intrinsic characteristics of the object, the acquired surface signals depend on the bandwidth of the measurement: the distribution of peaks and valleys in a surface profile is influenced

Figure 2. Part of the archaeological amphora with the scanned region highlighted.

Figure 3. 3D printed region of the amphora.

by the sampling step that, together with the Nyquist criterium, determines the smallest spatial structure.

Surface signal decomposition is of particular interest in archaeology, as the waviness pattern can be put in relation with the manufacturing tools. A polynomial fitting enables to separate the form and the texture to obtain the so-called conditioned surface (with zero mean), while the roughness is separated from the waviness using a Gaussian filter.

3.1. 3D printing

From the acquired data we can tailor the creation of a mesh to be used for reproducing the object with 3D printing technology. Most of the profilometers do not store the data as a point clouds or mesh so they cannot be printed directly. Therefore, we developed our own tools for building a mesh from the height maps collected by the microprofilometer. In detail, from the generated grid of equally spaced point we obtain the point cloud data with the triplet (X, Y, Z) representing the vertices of the mesh, we create the faces and hence a cuboid with the same dimension of the scan and we substitute the top face with the scan. Eventually, we can programmatically create and export the mesh to a STL file (using, for example, the Trimesh library [24]), the typical file format used by the 3D printers, storing the triangulated surface.

Figure 3 shows the 3D printed object, created using Stereolithography technology with a resolution of 50 μm in the z-axis of the printer. The resolution in the x-y printer plane is not specified even if it is specified the laser spot size of 140 μm [25].

In this kind of printing process, the object is printed layer-by-layer by polymerization of a liquid resin thanks to the exposure to laser light. Each single layer in the x-y plane is created by a raster-scanning of the focused laser light spot within the plane. The accuracy of the process depends also on the printing direction [26]. On this regard, it is worth to note that the best orientation of the model during the printing process should be the one that reflects the acquisition process. In fact, the optical microprofilometer is a line-of-sight technique that provides a height map as result of the measure and, like most of the conventional surface measurement techniques, it is not able to acquire re-entering features (like a "C-shape" along the scan directions).

4. SURFACE ANALYSIS AND COMPARISON

As mentioned above, a surface can be represented as a superimposition of different frequencies; adding a process in the chain can alter the resulting surface. In particular, the 3D printing process could be seen as a filter that cuts or badly passes some components. Therefore, the question to which we are interested,

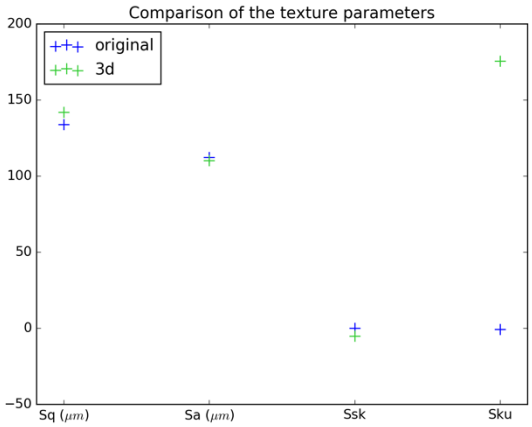

Figure 4. Comparison of amplitude parameters between original and 3D printed object: root mean square deviation (Sq), mean absolute deviation (Sa), skewness (Ssk) and kurtosis (Sku) of the surface heights distribution.

that naturally arises after the printing, regards the level of accuracy of the printing process in the creation of the replica.

To answer this question, the 3D printed object was scanned with the microprofilometer in the same measurement condition, i.e. with the same probe, lens, and scan velocity. The comparative analysis of the surfaces was performed on the basis of surface metrology parameters [27]-[30]. Figure 4 shows the comparison between the amplitude parameters of the original object and the 3D printed replica. In particular, the root mean square roughness *S*q, the average roughness *S*a, the skewness *S*sk and the kurtosis *S*ku are evaluated. It is worth noting that the *S*ku parameter, representing the sharpness of the surface peaks, deviates from -0.7 to 175.4, while the averaged texture amplitude *S*a varies from 112 μm to 110 μm, *S*q changes from 134 μm to 142 μm and the skewness *S*sk varies from 0 to -5.

In order to understand the differences between the surface datasets of the real object and the replica, the same signal decomposition is carried out, namely the form is separated from the texture through a second order polynomial fitting and then the roughness is highlighted through a Gaussian filter keeping the same parameters in both cases. The figures below (Figure 5, Figure 6) show the texture of the original and 3D printed objects.

Once the decomposition is done, the texture and the roughness are analysed using a multiscale approach [31]. This way, the texture and the roughness features are inspected with the variation of the observation scale. In order to have an insight of the average behaviour of the surface, the amplitude parameter *S*q and the extreme values parameters *S*z (maximum height of the peaks), *S*v (maximum depth of the valleys) and St (maximum peak to valley) are calculated as a function of the evaluation length. In particular, the multiscale analysis is developed as follows: the surface is divided in square subregions of specific side, i.e. the evaluation length, skipping a margin around the surface to avoid artefacts due to edge effects. In each subregion the aforementioned parameters are calculated and are then averaged on the patches. Plotting the texture parameters against the evaluation length gives an idea of their variation with the observation scale. Here, the evaluation length starts from 2 mm (400 sampled points in each subregion) and increases of 2 mm each time. From Figure 7 it emerges that the root mean square *S*q of the original and the 3D printed object follows a similar behaviour with the length scale. As expected, *S*q first increases with the evaluation length and then it converges to a stable value.

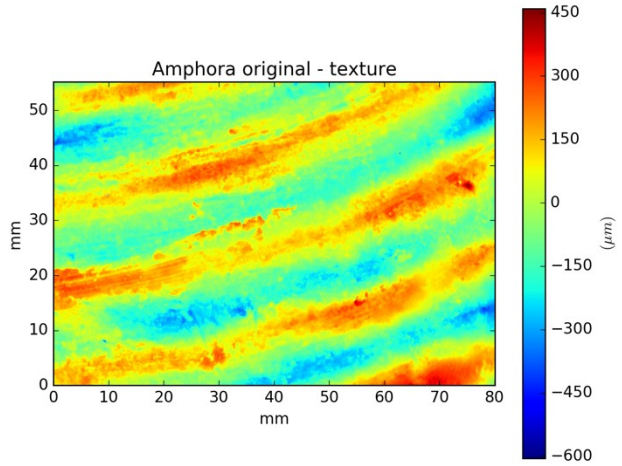

Figure 5. Texture of the original object acquired with a scan step of 100 µm and an accuracy in the z-axis of 10 µm.

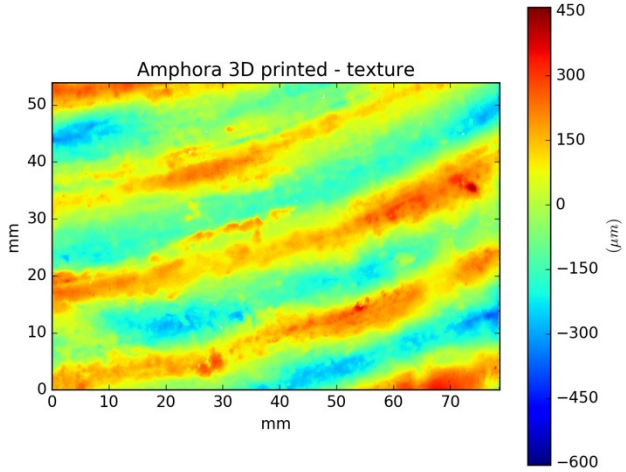

Figure 6. Texture of the 3D printed object acquired with a scan step of 100 µm and an accuracy in the z-axis of 10 µm.

Figures below show the variation of the extreme parameters with the evaluation length. As can be seen in Figure 8, the maximum peak to valley distance St follows a similar evolution, but it is interesting to note how the values regarding the 3D printed object are lower than those concerning the original

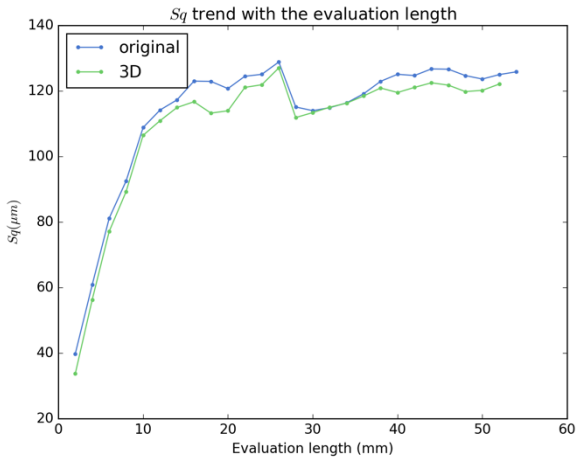

Figure 7. Variation of the Sq of the textures calculated at different scan size.

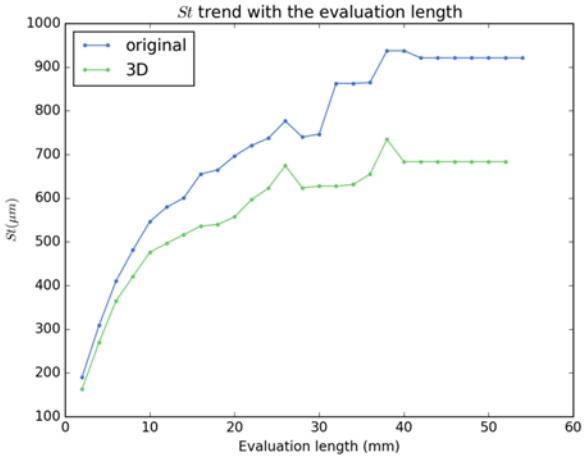

Figure 8. Variation of the peak-to-valley distances of the texture (*St*) calculated at different scan size.

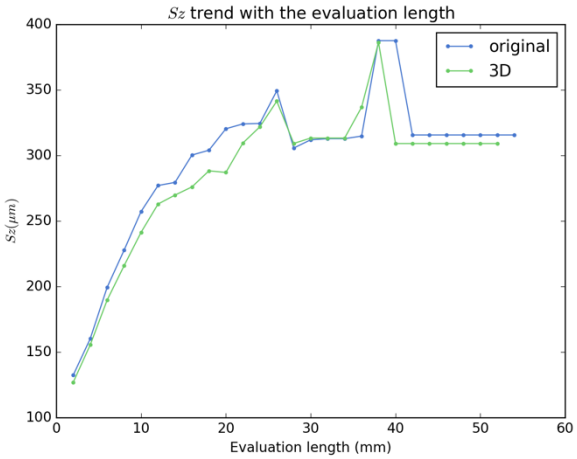

Figure 9. Variation of the maximum peak height of the texture (*Sz*) calculated at different scan size.

object. More in details, while the maximum height of the peaks *Sz* (Figure 9) has a similar trend, the maximum depth of valleys Sv (Figure 10) differs. Beside resolution limits, a possible explanation is the combined effects of the gravity and the washing that is performed after the 3D printing process. In fact, during the printing process, the object grew upside down and after the object was completed, it was subjected to washing and post-curing processes. The washing has the goal of removing uncured resin from the surface of printed parts by simultaneously soaking and moving them in a solvent, but it is possible that some particles of liquid remain trapped within the valleys.

Another comparative analysis was performed, in term of frequencies, through the Power Spectrum Density function (PSD). The PSD is calculated as the averaged one-dimensional PSDs along the scan direction of the surface height profiles. In order to have a double comparison, the PSD is calculated also in a second scan of the 3D printed object rotated of 180°.

The PSD is plotted versus the wavevectors defined as $q_i = 2\pi/\lambda_i$, where λ_i is the wavelength of the surface component.

Figure 11 shows the power spectrum of the whole surfaces while Figure 12 shows the power spectrum of the texture, i.e. the previous surfaces once the form is removed. As can be seen, the power spectrum of the total signal shows that the information is preserved for the lower frequencies, with a variation in the

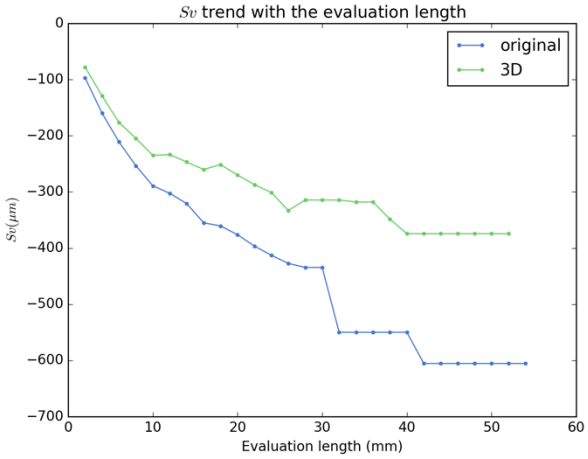

Figure 10. Variation of the maximum valley depth of the texture (*Sv*) calculated at different scan size.

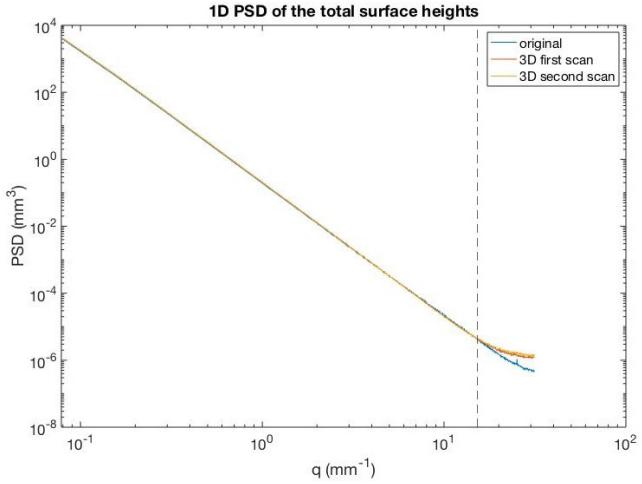

Figure 11. Comparison between the average power spectra of the total surface of original object and 3D printed object.

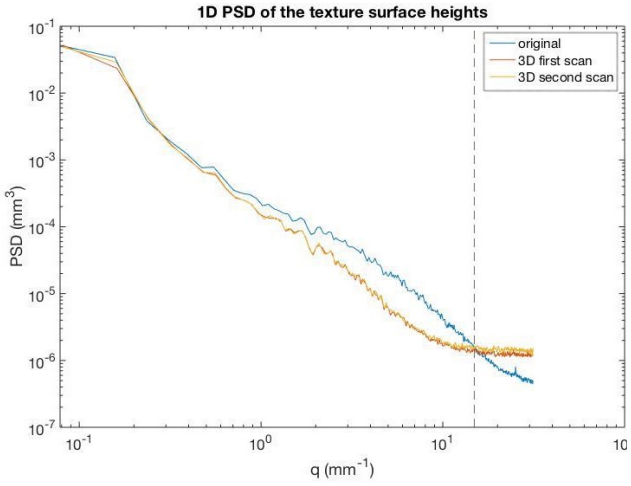

Figure 12. Comparison between the average power spectra of the texture signals of the original object and the 3D printed object.

behaviour of the higher frequencies at $q \approx 15\ \mathrm{mm}^{-1}$ ($\lambda \approx 0.42$ mm). This can be better analysed in the texture signal (Figure 12) where the power spectra of the real and printed objects intersect. Up to that point, the signal of the real object is higher, while from that point onward it emerges that the PSD of the printed object is no more informative.

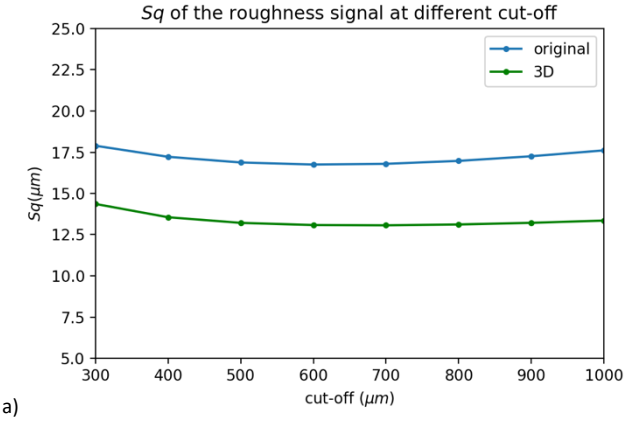

a)

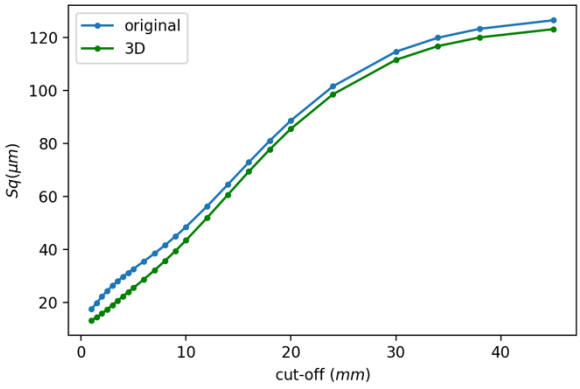

b)

Figure 13. Variation of the *Sq* with the cut-off wavelength of the Gaussian filter. The top plot a) represents the roughness signal extracted with a cut-off step of 100 μm while the second plot b) shows the increase in *Sq* by varying the cut-off from 1 mm to 45 mm.

The roughness analysis is done once the roughness signal is decomposed from the texture. The critical issues related to the use of the gaussian filter is the choice of the cut-off wavelength. The figure below shows the variation of *Sq* of the roughness signal of the original and the printed object versus the cut-off wavelength. As can be seen, the trend follows a similar behaviour with a lower *Sq* in the replica due the smoothing of the 3D printing process (Figure 13a). As the cut-off becomes longer, the *Sq* increases including also the waviness contribution (Figure 13b).

Figure 14 shows an example of the texture decomposition with a cut-off of 6 mm. It emerges that the waviness signal is well preserved while the roughness signal highlights the smoothing effect described above.

5. CONCLUSIONS

In this work we presented the application of scanning optical microprofilometry for the acquisition, the analysis, and the 3D printer reproduction of archaeological objects. Thanks to the capability to perform contact-less and full-field measurements with micrometric precision, this technique is a powerful tool for non-destructive testing and evaluation in cultural heritage. The versatile instrument configuration based on scanning stages and conoscopic holography sensors allows for setting optimal sampling parameters for different needs, enabling multiscale and multi-material surface measurements. The "field of view" of the

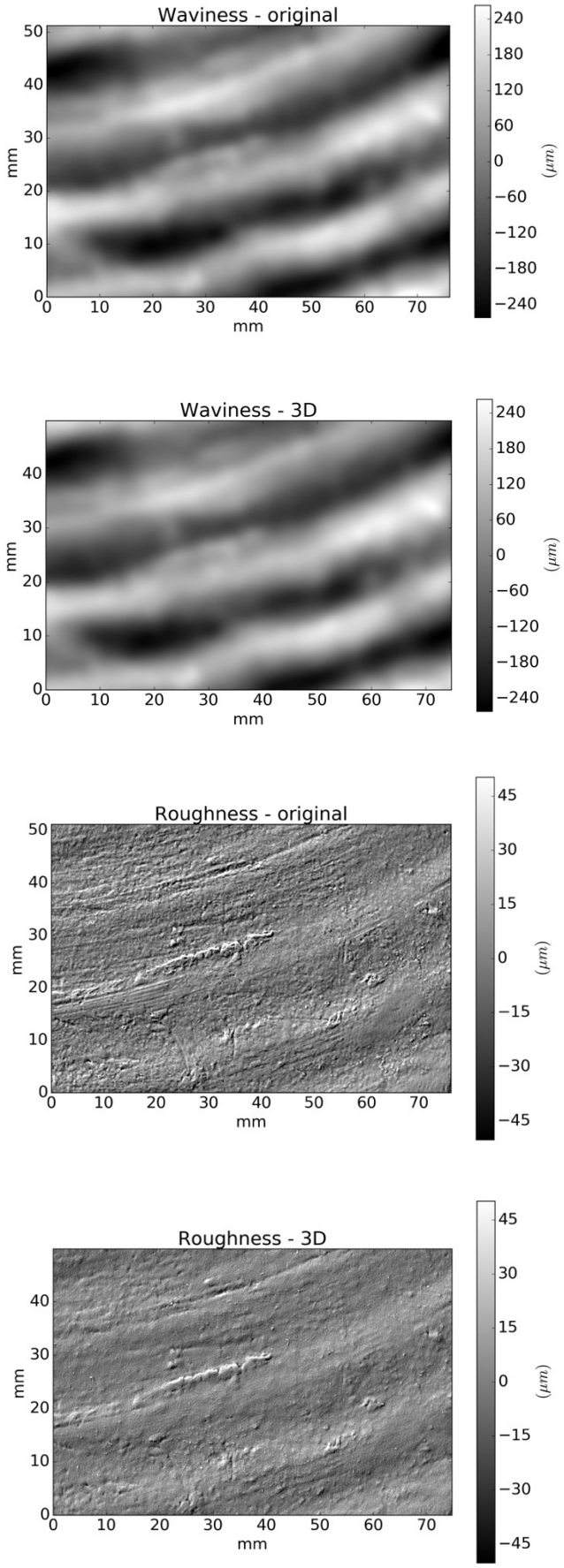

Figure 14. Surface signal decomposition: waviness with a cut-off of 6 mm and roughness with a cut-off of 600 μm.

X-Y scanning (up to 30 × 30 cm²) was designed for acquiring microsurface data in medium-sized objects, within a *Z* depth range that is determined by the lens (e.g. the range can vary from 0.6 mm to 180 mm maintaining the same probe), thus allowing the surface modelling of "flat" objects like ancient coins or significant part of 3D objects in a measuring session.

Reaching a micrometric resolution is of fundamental importance in the acquisition and in the analysis of the material surface. In this study we focused on the measurement of an archaeological object representing a complex and exemplar case study, with sharp evidence of the three main surface signal components: shape, waviness, and roughness. We demonstrated how we obtained a high-fidelity and high-resolution 3D printed replica of the object starting from the microprofilometry dataset. Moreover, we have come full circle acquiring the printed object and assessing how the process preserves the surface signals. In order to perform this task, a multiscale analysis of the original and 3D printed object is proposed by inspecting the inband roughness through the power spectrum, as well as the variation of the areal amplitude parameters (*Sa*, *Sq*, *Ssk*, and *Sku*) with the observation length. It was demonstrated how the printing process is accurate even if the replica is affected by less marked valleys and by a loss of signal in the high frequency surface components, thus resulting in a smoothing effect. Using a scanning step of 100 μm in the microprofilometer with the conoscopic probe setting a laser spot of 47 μm and a depth accuracy of 10 μm, and using a printing resolution of 50 μm (along the printer z-axis), it is shown that, beside the form of the archaeological manufact, the surface texture is accurately acquired and 3D printed without artifacts affecting the waviness and the roughness appearance.

The focus of this work was the feasibility and performance analysis in 3D printing of artworks using laser scanning microprofilometry. We have turned our attention to a 3D replica obtained with the stereolithography technology and a photopolymer resin. However, the method could be used to compare the performance of different kind of 3D printer technologies as well as various orientation settings of the model during the printing process or several printers-resin combinations.

ACKNOWLEDGEMENT

The work was partly supported by SCAN4RECO project funded by the European Union Horizon 2020 Framework Programme for Research and Innovation under grant agreement no 665091 and partly by TEMART project, POR FESR 2014-2020.

REFERENCES

[1] G. Sansoni, M. Trebeschi, F. Docchio, State-of-The-Art and Applications of 3D Imaging Sensors in Industry, Cultural Heritage, Medicine, and Criminal Investigation, Sensors, vol. 9, no. 1, Jan. 2009, pp. 568–601. DOI: 10.3390/s90100568

[2] C. Balletti, M. Ballarin, F. Guerra, 3D printing: State of the art and future perspectives, J. Cult. Herit., vol. 26, Jul. 2017, pp. 172–182. DOI: 10.1016/j.culher.2017.02.010

[3] Yu Ying Clarrisa Choong, Hong Wei Tan, Deven C. Patel, Wan Ting Natalie Choong, Chun-Hsien Chen, Hong Yee Low, Ming Jen Tan, Chandrakant D. Patel, Chee Kai Chua, The global rise of 3D printing during the COVID-19 pandemic, Nat. Rev. Mater., vol. 5, no. 9, Sep. 2020, pp. 637–639. DOI: 10.1038/s41578-020-00234-3

[4] V. M. Vaz L. Kumar, 3D Printing as a Promising Tool in Personalized Medicine, AAPS PharmSciTech, vol. 22, no. 1, Jan. 2021, p. 49.
DOI: 10.1208/s12249-020-01905-8
[5] T. Singh, S. Kumar, S. Sehgal, 3D printing of engineering materials: A state of the art review, Mater. Today Proc., vol. 28, 2020, pp. 1927–1931.
DOI: 10.1016/j.matpr.2020.05.334
[6] R. Scopigno, P. Cignoni, N. Pietroni, M. Callieri, M. Dellepiane, Digital Fabrication Techniques for Cultural Heritage: A Survey, Comput. Graph. Forum, vol. 36, no. 1, Jan. 2017, pp. 6–21.
DOI: 10.1111/cgf.12781
[7] Balletti Ballarin, An Application of Integrated 3D Technologies for Replicas in Cultural Heritage, ISPRS Int. J. Geo-Information, vol. 8, no. 6, Jun. 2019, p. 285.
DOI: 10.3390/ijgi8060285
[8] S. Mazzocato C. Daffara, Experiencing the Untouchable: A Method for Scientific Exploration and Haptic Fruition of Artworks Microsurface Based on Optical Scanning Profilometry, Sensors, vol. 21, no. 13, Jun. 2021, p. 4311.
DOI: 10.3390/s21134311
[9] G. Schirripa Spagnolo, L. Cozzella, F. Leccese, Fringe projection profilometry for recovering 2.5D shape of ancient coins, Acta IMEKO, vol. 10, no. 1, Mar. 2021, p. 142.
DOI: 10.21014/acta_imeko.v10i1.872
[10] P. Dondi, L. Lombardi, M. Malagodi, M. Licchelli, 3D modelling and measurements of historical violins, Acta IMEKO, vol. 6, no. 3, p. 29, Sep. 2017.
DOI: 10.21014/acta_imeko.v6i3.455
[11] R. Fontana et al., Three-dimensional modelling of statues: the Minerva of Arezzo, J. Cult. Herit., vol. 3, no. 4, Oct. 2002, pp. 325–331.
DOI: 10.1016/s1296-2074(02)01242-6
[12] F. Remondino, Heritage Recording and 3D Modeling with Photogrammetry and 3D Scanning, Remote Sens., vol. 3, no. 6, May 2011, pp. 1104–1138.
DOI: 10.3390/rs3061104
[13] A. Mironova, F. Robache, R. Deltombe, R. Guibert, L. Nys, M. Bigerelle, Digital Cultural Heritage Preservation in Art Painting: A Surface Roughness Approach to the Brush Strokes, Sensors, vol. 20, no. 21, Nov. 2020, p. 6269.
DOI: 10.3390/s20216269
[14] M. Callieri et al., Alchemy in 3D: A digitization for a journey through matter, in 2015 Digital Heritage, Sep. 2015, pp. 223–230.
DOI: 10.1109/digitalheritage.2015.7413875
[15] J. Striova, L. Pezzati, E. Pampaloni, R. Fontana, Synchronized Hardware-Registered VIS-NIR Imaging Spectroscopy and 3D Sensing on a Fresco by Botticelli, Sensors, vol. 21, no. 4, Feb. 2021, p. 1287.
DOI: 10.3390/s21041287
[16] E. George, P. Liacouras, F. J. Rybicki, D. Mitsouras, Measuring and Establishing the Accuracy and Reproducibility of 3D Printed Medical Models, RadioGraphics, vol. 37, no. 5, pp. 1424–1450, Sep. 2017.
DOI: 10.1148/rg.2017160165
[17] E. Kluska, P. Gruda, N. Majca-Nowak, The Accuracy and the Printing Resolution Comparison of Different 3D Printing Technologies, Trans. Aerosp. Res., vol. 2018, no. 3, Sep. 2018, pp. 69–86.
DOI: 10.2478/tar-2018-0023
[18] R. M. Carew, R. M. Morgan, C. Rando, A Preliminary Investigation into the Accuracy of 3D Modeling and 3D Printing in Forensic Anthropology Evidence Reconstruction, J. Forensic Sci., vol. 64, no. 2, Mar. 2019, pp. 342–352.
DOI: 10.1111/1556-4029.13917
[19] V. Bonora, G. Tucci, A. Meucci, B. Pagnini, Photogrammetry and 3D Printing for Marble Statues Replicas: Critical Issues and Assessment, Sustainability, vol. 13, no. 2, Jan. 2021, p. 680.
DOI: 10.3390/su13020680
[20] N. Gaburro, G. Marchioro, C. Daffara, A versatile optical profilometer based on conoscopic holography sensors for acquisition of specular and diffusive surfaces in artworks, Jul. 2017, p. 103310A.
DOI: 10.1117/12.2270307
[21] N. Gaburro, G. Marchioro, C. Daffara, Conoscopic laser microprofilometry for 3D digital reconstruction of surfaces with sub-millimeter resolution, in 2017 IEEE International Conference on Environment and Electrical Engineering and 2017 IEEE Industrial and Commercial Power Systems Europe (EEEIC / I&CPS Europe), Jun. 2017, pp. 1–4.
DOI: 10.1109/eeeic.2017.7977779
[22] G. Y. Sirat, Conoscopic holography I Basic principles and physical basis, J. Opt. Soc. Am. A, vol. 9, no. 1, Jan. 1992, p. 70.
DOI: 10.1364/josaa.9.000070
[23] I. Álvarez, J. Enguita, M. Frade, J. Marina, G. Ojea, On-Line Metrology with Conoscopic Holography: Beyond Triangulation, Sensors, vol. 9, no. 9, Sep. 2009, pp. 7021–7037.
DOI: 10.3390/s90907021
[24] Trimesh [Computer software]. Online [Accessed 23 March 2022] https://trimsh.org/
[25] Formlabs, Form2 Tech Specs. Online [Accessed 23 March 2022] https://formlabs.com/3d-printers/form-2/tech-specs/
[26] T. Hada et al., Effect of Printing Direction on the Accuracy of 3D-Printed Dentures Using Stereolithography Technology, Materials (Basel)., vol. 13, no. 15, Aug. 2020, p. 3405.
DOI: 10.3390/ma13153405
[27] International Organization for Standardization, ISO 25178-1:2016, Geometrical product specifications (GPS) — Surface texture: Areal — Part 1: Indication of surface texture, Geneva, 2016.
[28] International Organization for Standardization, ISO 25178-2:2012, Geometrical product specifications (GPS) — Surface texture: Areal — Part 2: Terms, definitions and surface texture parameters, Geneva, 2012.
[29] International Organization for Standardization, ISO 25178-3:2012, Geometrical product specifications (GPS) — Surface texture: Areal — Part 3: Specification operators, Geneva, 2012.
[30] F. Blateyron, The Areal Field Parameters, in Characterisation of Areal Surface Texture, Berlin, Heidelberg: Springer Berlin Heidelberg, 2013, pp. 15–43.
DOI: 10.1007/978-3-642-36458-7_2
[31] M. Bigerelle, T. Mathia, S. Bouvier, The multi-scale roughness analyses and modeling of abrasion with the grit size effect on ground surfaces, Wear, vol. 286–287, May 2012, pp. 124–135.
DOI: 10.1016/j.wear.2011.08.006